Original Contribution

H-Scan Discrimination for Tumor Microenvironmental Heterogeneity in Melanoma

Jihye Baek [a], Shuyang S. Qin [b], Peter A. Prieto [c], Kevin J. Parker [a,*]

[a] Department of Electrical and Computer Engineering, University of Rochester, Rochester, NY, USA
[b] Department of Microbiology & Immunology, University of Rochester School of Medicine & Dentistry, Rochester, NY, USA
[c] Department of Surgery, University of Rochester Medical Center, Rochester, NY, USA

Objective: Melanoma is a form of malignant skin cancer that exhibits significant inter-tumoral differences in the tumor microenvironment (TME) secondary to genetic mutations. The heterogeneity may be subtle but can complicate the treatment of metastatic melanoma, contributing to a high mortality rate. Therefore, developing an accurate and non-invasive procedure to discriminate microenvironmental heterogeneity to facilitate therapy selection is an important goal.
Methods: In vivo murine melanoma models that recapitulate human disease using synchronous implanted YUMM 1.7 (Yale University Mouse Melanoma) and YUMMER 1.7 (Yale University Mouse Melanoma Exposed to Radiation) murine melanoma lines were investigated. Mice were treated with antibodies to modulate the immune response and longitudinally scanned with ultrasound (US). US radiofrequency data were processed using the H-scan analysis, attenuation estimation and B-mode processing to extract five US features. The measures were used to compare different TMEs (YUMMER vs. YUMM) and responses to immunomodulatory therapies with CD8 depletion or programmed cell death protein 1 (PD-1) inhibition.
Results: Multiparametric analysis produced a combined H-scan parameter, resolving significant differences (i) between untreated YUMMER and YUMM and (ii) between untreated, PD-1-treated and CD8-treated YUMMER. However, more importantly, the B-mode and attenuation measures failed to differentiate YUMMER and YUMM and to monitor treatment responses, indicating that H-scan is required to differentiate subtle differences within the TME.
Conclusion: We anticipate that the H-scan analysis could discriminate heterogeneous melanoma metastases and guide diagnosis and treatment selection, potentially reducing the need for invasive biopsies or immunologic procedures.

Introduction

Medical ultrasound (US) has been widely used to diagnose and screen diseases, including liver steatosis/fibrosis/tumors, kidney fibrosis and breast cancer. Usage of US has increased because of its numerous advantages: it is non-invasive, it provides real-time imaging, it can be portable and it is lower in cost compared with magnetic resonance imaging (MRI) and computed tomography (CT). However, US traditionally has limited usage in disease diagnosis because its qualitative imaging display relies on clinicians' interpretations. Further, traditional B-mode images alone cannot detect subtle pathologic changes in tissues. B-mode imaging also has lower diagnostic performance than MRI or CT [1], which motivates the development of methodologies that extract more information from raw US signals. Recently, quantitative US (QUS) has been introduced to provide quantitative measures from US scans [2], which enabled diagnostic improvement compared with traditional B-

mode imaging in many applications such as cancer and disease detection, disease progression monitoring and treatment response tracking [3−5]. The diagnostic accuracy of QUS can be verified using accepted measures from pathology or MRI. For steatosis, MRI-driven proton density fat fraction (MRI-PDFF) is known as one of the accurate approaches among non-invasive imaging modalities [6−10]. Thus, QUS parameters extracted from steatosis human participants were compared with MRI-PDFF and exhibited high correlation [5]. Although QUS studies include spectral based analysis, another US frequency-dependent analysis of the H-scan has been proposed [11,12]. The H-scan uses a matched filter analysis to characterize scattering behavior and provides color-coded images to visualize different categories of scatterers. The H-scan has been applied to liver imaging to monitor pancreatic cancer metastasis [13]. That study determined that the H-scan results strongly agreed with biofluorescence measurements and performed better compared with US measurements of shear wave speed. Moreover, it has been revealed that

H-scan measures have high correlations with pathology or MRI-PDFF in assessment of many diseases, including liver steatosis (correlation coefficients: $R = 0.83$ with histology fat fraction [14] and $R = 0.86$ with MRI-PDFF [15]), kidney fibrosis ($R = 0.99$ with histology fibrosis score [16]) and breast cancer (area under the curve = 0.81 with biopsy). These findings suggested the potential of H-scan to contribute diagnosis based on US quantitative measurements.

As a great number of quantitative parameters have been introduced to identify tissue characteristics, the integration of multiple parameters may improve characterization accuracy. Thus, multiparametric analysis was suggested with several approaches: (i) non-linear transformation to calculate a combined parameter [17], (ii) support vector machine (SVM) to incorporate information from parameters [18,19] and (iii) principal component analysis and inner product to obtain a 1-D combined parameter [14]. These studies demonstrated that incorporating multiple parameters improved differentiation between different stages of disease, for example, (i) normal versus inflammation versus fibrosis in the liver [18], (ii) normal versus steatosis in the liver [20] and (iii) benign versus malignant breast lesion [21,22]. Moreover, these studies found that the H-scan was one of the most accurate contributors to tissue classification.

Although previous studies investigated different disease conditions, the efficacy of US in discriminating subtypes of the same disease remained unknown. Inter-tumoral heterogeneity in metastatic melanoma is a clinically relevant phenomenon that requires such distinction. Metastatic melanoma patients have an average survival rate of less than 6 mo [23]. One contributor to mortality rate may be heterogenous treatment responses and different metastases exhibited within the same individual secondary to genetic and tumor microenvironment (TME) variations between the two lesions [24,25].

To study tumor heterogeneity in melanoma, murine models of melanoma have previously been developed: the Yale University Mouse Melanoma line, known as YUMM 1.7 (YUMM), and the Yale University Mouse Melanoma Exposed to Radiation, known as YUMMER 1.7 (YUMMER). These cell lines are used to recapitulate the genetic and TME heterogeneity [25]. The YUMM and YUMMER cell lines share 37% of synchronous mutations [26], which created immunologically distinct TMEs, with YUMMER having increased immune infiltration compared with YUMM [25]. Detection of the distinct subtypes requires an invasive biopsy for comprehensive analyses such as immunohistochemistry, Luminex analyte assay and RNA sequencing; these biopsies are typically clinically cost inefficient. However, given the effect of immunologically distinct TME on melanoma therapy response, non-invasive measures are needed to identify immunologic properties of metastases to improve therapy selection.

In this study, we used non-invasive H-scan US approaches to detect TME heterogeneity in a murine model of melanoma with implanted YUMM or YUMMER tumors. To study the efficiency of H-scan on differentiating immunologic differences in the TME, YUMM and YUMMER tumors were treated with either anti-CD8 antibodies, which decrease the amount of intra-tumoral immune infiltration, or with anti-PD-1 (programmed cell death protein 1) antibodies, which increase immune infiltration. The H-scan analysis was performed to discriminate YUMM and YUMMER and to monitor treatment responses over time. H-scan parameters and US parameters were measured, and a multiparametric analysis was performed to combine parameter information.

Methods

Study design

This study protocol was approved by the University of Rochester's University Committee on Animal Resources. The bilateral flanks of 6- to 8-wk-old female wild-type C57BL/6J mice from the Jackson Laboratory (Bar Harbor, ME, USA) were injected with one million YUMM 1.7 or YUMMER 1.7 cells [25]. The implanted murine melanoma tumors were
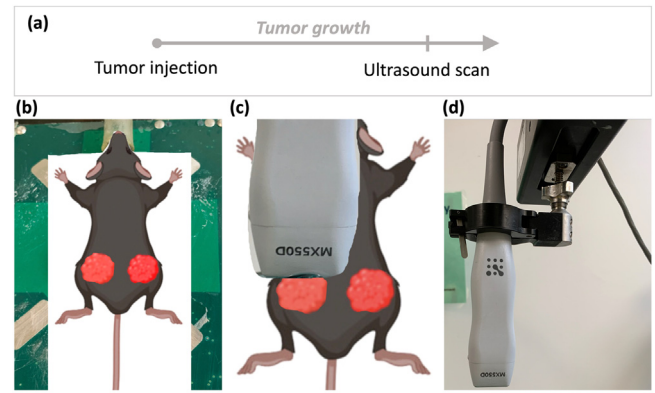

Figure 1. Murine melanoma model study design and experimental setup. (a) Tumor injection in mice flanks, tumor growth and ultrasound scan. (b) An anesthetized mouse with two induced tumors on both sides of flanks before ultrasound scanning. (c) Scanning a grown tumor with ultrasound gel. (d) Three-dimensional scan performed with a mechanical motion controller.

US-scanned, as illustrated in Figure 1. Mice were split into isotype antibody-treated control, anti-PD-1-treated and CD8-depleted groups to represent baseline immune infiltration, increased immune infiltration and decreased immune infiltration, respectively. The mice received treatment three times per week once the tumors reached 4 mm in the largest diameter and were sacrificed on day 27 post-tumor implantation; for all tumors, the largest diameter was between 4 and 2 mm at the time of scanning. Tumors subsequently underwent hematoxylin and eosin (H&E) histologic staining and CD45 immunohistochemical staining.

US acquisitions

Ultrasound scanning was performed using the Vevo 3100 imaging system (FUJIFILM VisualSonics, Inc., Toronto, ON, Canada) equipped with a 40 MHz center frequency linear transducer (MX550D). Focused beam transmission was used, and a single focal depth of 10 mm was set for all scans. We acquired 3-D volume images with a 0.05 mm step size between 2-D frames, and the acquired volumes had approximately 0.1 to 5 mm lengths depending on tumor size, whereby each 3-D volume data point had approximately 2 to 100 frames; the 3-D scan with the linear transducer was performed with a mechanical motion controller, as illustrated in Figure 1d. The machine saved radiofrequency (RF) data, and we produced B-mode images by in-phase and quadrature (IQ) demodulation, envelope detection and log compression. The B-mode images were used for manual contouring of the melanoma boundary for each frame, which was the region of interest (ROI) for this study, indicating the melanoma area. The saved RF data format was used for H-scan processing and attenuation correction, and envelope and log-compressed data were used to measure intensity-based parameters.

We estimated two B-scan parameters: B-scan intensity and B-scan signal-to-noise ratio (SNR). First, B-scan intensity was obtained by averaging the decibel scale intensity of log-compressed data within the contoured ROI. B-scan SNR was calculated using the envelope data:

$$B - \text{scan SNR} = \frac{\mu_\text{B}}{\sigma_\text{B}} \tag{1}$$

Here, μ_B and σ_B are the average and standard deviation of the envelope data within an ROI, respectively. When estimating the two B-scan parameters, as illustrated in Figure 2, we excluded any area having US artifacts, such as reverberation artifacts, shadowing and non-uniform US beam energy in the depth direction caused by focused transmission. Our scan setting with a single focus at 10 mm reduced the SNR at deeper depths compared with the focal point, and thus our parameter estimation occurred at depths less than 11 mm. All scanlines and samples
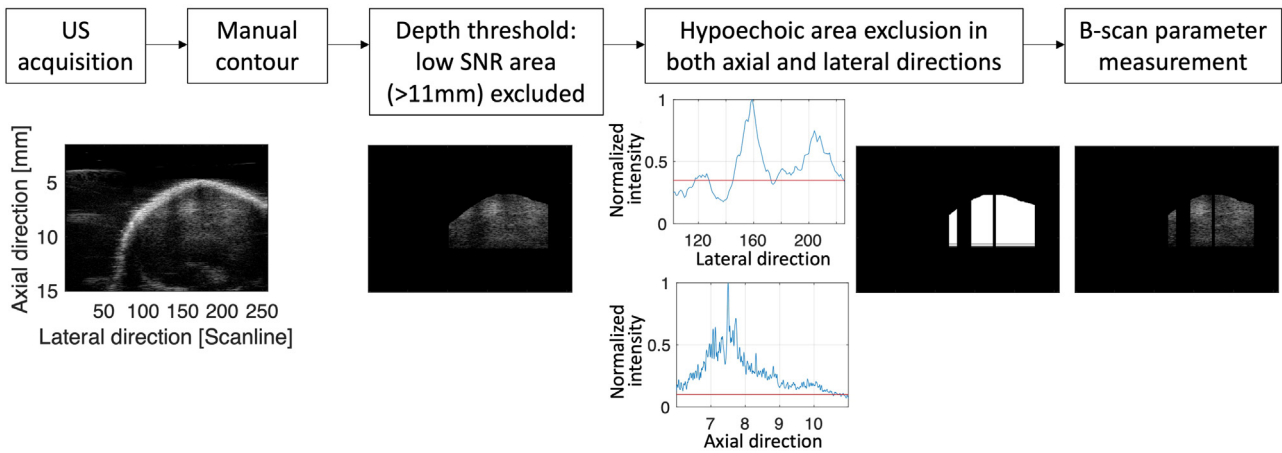
Figure 2. Exclusion of hypo-echoic (low signal) area to estimate B-scan parameters. US, ultrasound.

having reverberation artifacts or shadowing were excluded from the estimation by defining lateral and axial intensity thresholds, as depicted in Figure 2. Figure 2 also illustrates a mask example and US B-scan speckle within the mask.

H-scan analysis

We extracted features from the RF data frequency using the H-scan analysis [12]. The H-scan was performed to investigate frequency spectral shifts caused by attenuation or scatterer size changes. The process is summarized in Figure 3. First, US RF data were acquired and used as input for the H-scan. Because US propagation causes frequency downshifts along depth, leading to confusion between the attenuation effects and scattering signature changes we aim to detect, attenuation correction was performed. The frequency-dependent attenuation can be modeled by $e^{-\alpha fx}$, where α is attenuation coefficient (in Np/cm), f is frequency (in MHz) and x is depth (in cm). Conceptually, by multiplying $e^{+\alpha fx}$ by the frequency spectrum $S(f) = fft\left(RF(x)\right)$, we can obtain attenuation-corrected (ac) RF data (RF^{ac}):

$$RF^{ac} = ifft\left(S(f) \cdot e^{+\alpha fx}\right) \qquad (2)$$

Equation (2), however, contains two variables, frequency f and depth x. To make the depth variable a constant, we divided the depth ROI into 10 zones, and each zone z had a representative depth x_z. Now, a simple calculation of attenuation-corrected RF data is possible with $S(f) \cdot e^{+\alpha f x_z}$, and each zone's attenuation-corrected RF data is $RF_z^{ac}(t) = S(f) \cdot e^{+\alpha f x_z}$. To obtain the attenuation-corrected RF data RF$^{ac}(t)$ over the entire depth range/zones, RF$_z^{ac}(t)$ can be combined. The attenuation equation $e^{-\alpha fx}$ also describes intensity attenuation, although most US machines provide RF data after time-gain compensation (TGC), so $S(f) \cdot e^{+\alpha fx}$ compensates for intensity attenuation. Thus, before combining, intensity normalization between zones is needed only if the RF data were acquired after TGC. The H-scan processing used attenuation-corrected RF data: $RF^{ac}(t)$. For matched filtering, 256 Gaussian filters (G_i for $i = 1, 2, \ldots, 256$) were determined with different peak frequencies: f_{p_i} for $i = 1, 2, \ldots, 256$, where $f_{p\_1} < f_{p\_2} < \ldots < f_{p\_256}$ and $f_{p\_k+1} - f_{p\_k} = \Delta f$. Δf is a constant that can be defined based on the frequency spectrum of the RF data for all peak frequencies to cover the entire spectrum from low- to high-frequency components. A bandwidth of the Gaussian filters was specified by a standard deviation, σ_G, as detailed in Figure 3. The bandwidth of Gaussian filters was set to have 70% of the spectral bandwidth; we first estimated an averaged standard deviation of frequency spectra for RF data (σ_{RF}) to find the bandwidth, and the bandwidths of the Gaussian filters were determined by $\sigma_G = \sigma_{RF} \cdot 0.7$. Bandpass filtering between the Fourier transform of RF data and the Gaussian filters was performed,
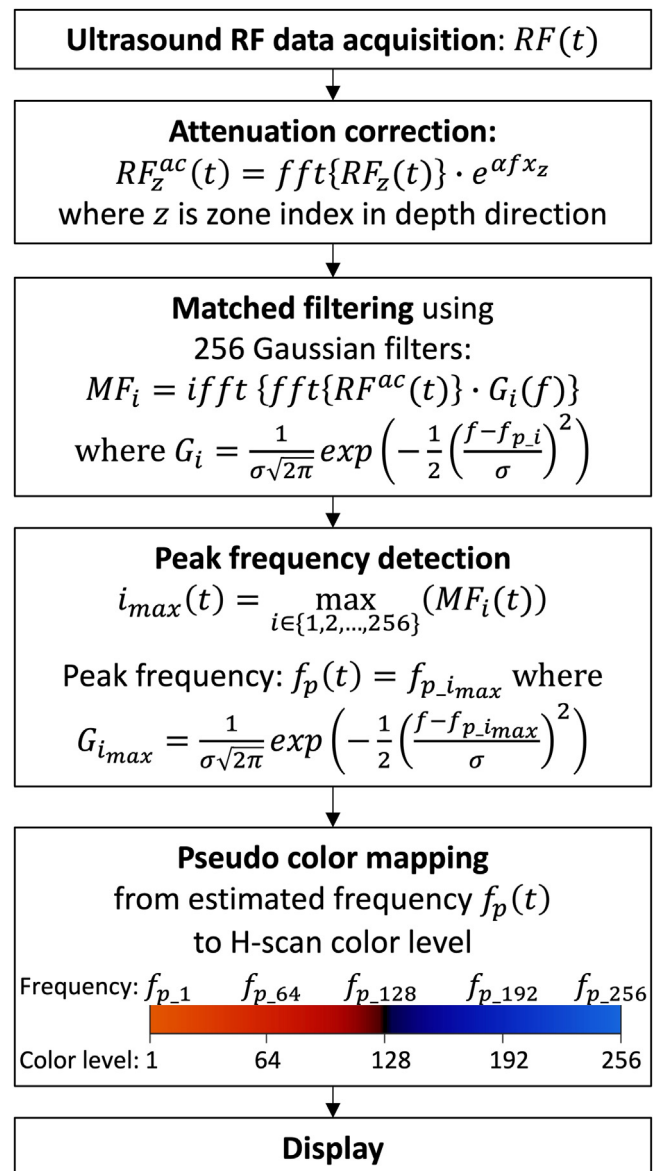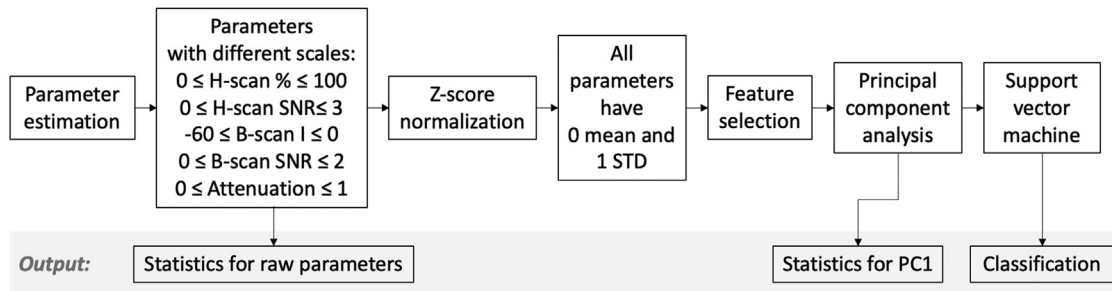

Figure 3. H-scan processing.

Figure 4. Multiparametric analysis to combine information from parameters.

and the 256 outputs were inverse Fourier-transformed, resulting in 256 outputs of the matched filtering: MF_i for $i = 1, 2, \ldots, 256$. Note that convolution in the time domain can be used instead of bandpass filtering in the frequency domain. After the filtering, each time sample t in the axial direction (each pixel in 2-D US images) had 256 values: $MF_1(t)$, $MF_2(t), \ldots, MF_{256}(t)$. We can find a unique maximum of $MF_{i_{max}}(t)$ where i_{max} is the index of the Gaussian filter $G_{i_{max}}$, and $G_{i_{max}}$ has a peak frequency $f_{p\_i_{max}}$ as shown in Figure 3. Then $f_{p\_i_{max}}$ is the estimated frequency component at time sample t: $f_p(t) = f_{p\_i_{max}}$. The estimated frequency components were mapped into H-scan color levels using the color bar shown in the pseudo color mapping block in Figure 3. The H-scan color levels from 1 to 256 are depicted as more red to more blue, in order, as shown in the color bar in Figure 3. The redder color indicates low-frequency components and larger scatterers, corresponding to the lower color levels. Thus, the H-scan estimates a color level for each pixel within a ROI. As the color levels range from 1 to 256, the color levels from 1 to 128 were classified as red pixels, and those from 129 to 256 were classified as blue pixels. We defined H-scan blue percentages (H-scan % blue) as

$$H - scan\ \%\ blue = \frac{Number\ of\ blue\ pixels}{Total\ number\ of\ pixels\ within\ ROI} \times 100\% \qquad (3)$$

We calculated H-scan SNR as

$$H - scan\ SNR = \frac{\mu_H}{\sigma_H} \qquad (4)$$

where μ_H and σ_H are the average and standard deviation of the H-scan color levels within a ROI, respectively.

As previously mentioned, when using raw RF data as the H-scan input, the attenuation effect of the frequency downshift can be detected, with more red color for deeper depths. We estimated attenuation coefficients using the H-scan blocks in Figure 3. Attenuation estimation used raw RF data before attenuation correction. Through the matched filtering and peak frequency detection blocks, peak frequency ($f_p(x)$) along depth (x) was estimated, and the attenuation coefficient ($\widehat{\alpha}(x)$ [dB/MHz/cm]) can be calculated as

$$\widehat{\alpha}(x) = -\frac{f_p(x) - f_0}{x \cdot \sigma^2} \qquad (5)$$

where f_0 is center frequency and σ is the bandwidth of the transmit US beam. More details on attenuation estimation, including eqn (5), are found in Baek et al. [19]. In this study, we first estimated the attenuation coefficient, and then used the estimated attenuation coefficient for attenuation correction.

Multiparametric analysis

For multiparametric analysis, we estimated five parameters: two B-scan parameters (B-scan intensity and B-scan SNR) based on US backscattering, two H-scan parameters (H-scan % blue and H-scan SNR) extracted from US frequency-dependent information and the attenuation coefficient reflected by US physics. Through multiparametric analysis,

the best-performing parameters were selected and combined; detailed procedures are provided in Figure 4.

As illustrated in Figure 4, the extracted raw parameters had different scales. Z-score normalization was performed to obtain a 0 mean and 1 standard deviation, which enabled a reasonable comparison between parameters with a consistent scale and distribution. Feature selection was performed by investigating possible parameter combinations, such as all five parameters, four parameters after excluding only one, three parameters after excluding two and two parameters. For each of the possible combinations, principal component analysis (PCA) was used to calculate the first and second principal components (PC1 and PC2, respectively). PC1 is considered a combined parameter for statistical analysis. One-way analysis of variance (ANOVA) was used to evaluate differentiation between (i) distinct melanoma models (YUMMER and YUMM) and (ii) treatment conditions (untreated, PD-1 and CD8). Moreover, to visualize clusters in 2-D space, SVM classification was performed. On the basis of the p value from ANOVA and the classification accuracy from SVM, the best-performing parameter combination for melanoma discrimination included solely the two H-scan parameters. Therefore, from the normalized H-scan % blue and SNR, PCA calculated the first and second principal components, PC1 and PC2, respectively. PC1 is a combined parameter resulting from combining information through multiparametric analysis, and further, to visualize the results, SVM classification was applied to PC1 and PC2.

Results

YUMMER versus YUMM

We subcutaneously implanted the murine melanoma cell line YUMM or YUMMER into the mice flanks to generate an animal model of melanoma. A previous study [25] had determined that these two cell lines established immunologically distinct TMEs in vivo with YUMMER tumors having significantly more immune cells than YUMM (Fig. 5). In Figure 5a−d, the smaller and darker cells likely represent immune cells, whereas the larger cells represent tumor and stromal cells. Immunohistologic staining for CD45+, a marker for immune cells, confirmed increased CD45+ immune infiltration in YUMMER tumors compared with YUMM tumors (Fig. 5e, 5f).

We measured the following five parameters from US data: H-scan % blue, H-scan SNR, B-scan intensity, B-scan SNR and the attenuation coefficient. To exclude outliers, we included only measurements that are in the range within two standard deviations for each parameter, when analyzing the measures for statistical analysis and classifications. The results are provided in Figure 6, and only the H-scan parameters were able to distinguish the immunologically distinct TMEs, revealing significantly different measurements between YUMMER and YUMM tumors: $p < 0.01$ for H-scan % blue and $p < 0.05$ for H-scan SNR. According to the Figure 6a H-scan results, YUMMER tumors had a higher percentage of blue pixels, meaning that a greater number of smaller scatterers were detected in YUMMER than in YUMM tumors. This finding is consistent
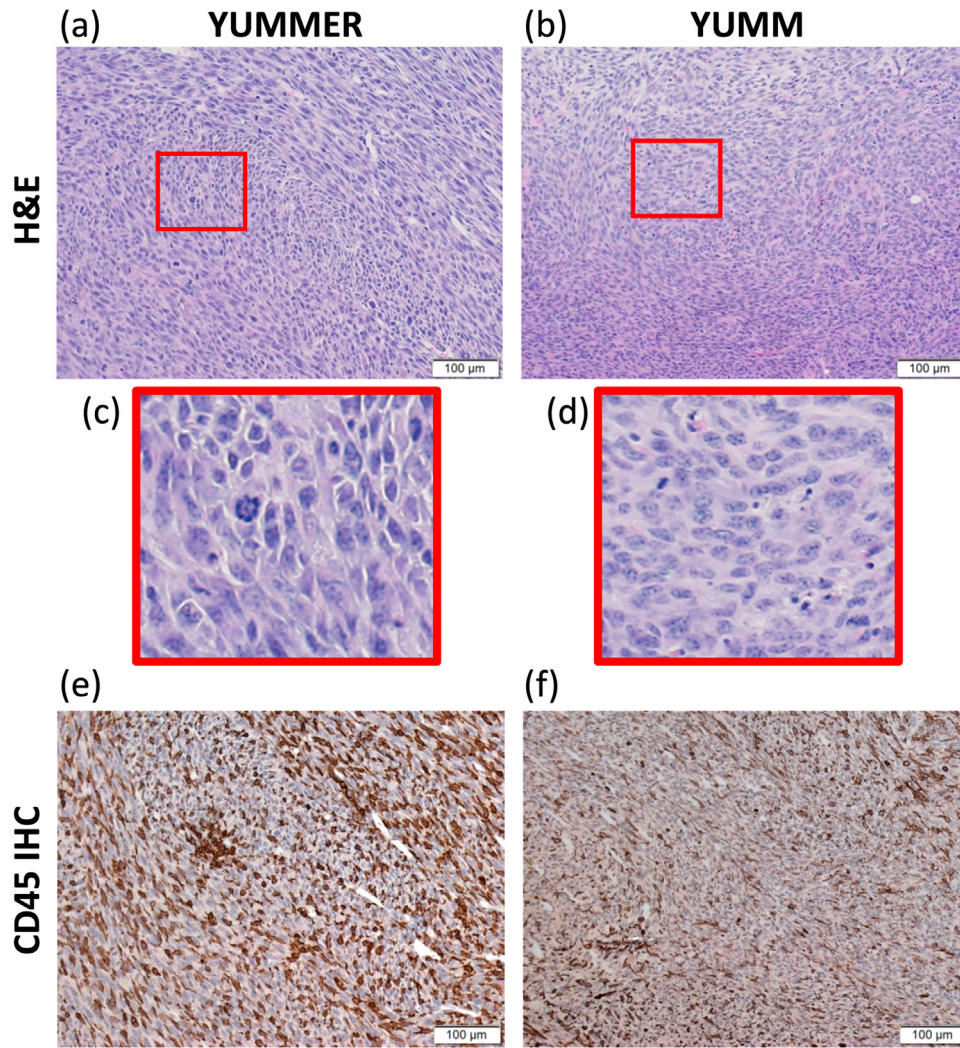
Figure 5. Representative (a−d) histology images stained with hematoxylin and eosin (H&E) and (e, f) CD45 immunohistochemistry (IHC) for (a, c, e) YUMMER and (b, d, f) YUMM tumors. The red region of interest (ROI) boxes in (a) and (b) were magnified into (c) and (d), respectively.

with the histology, which revealed higher infiltration of smaller immune cells in YUMMER tumors (Fig. 5).

In are representative B-scan and H-scan images for YUMMER and YUMM tumors. The YUMMER tumor H-scan image clearly revealed more blue pixels than the YUMM tumor H-scan. Because of the increase in smaller immune cells in YUMMER tumors, their H-scan results were more blue than those of the YUMM lesions. Also, blue pixels tended to be found near the boundary, which may represent peritumoral

infiltration of immune cells, a common clinical phenomenon present in solid tumors.

Treatment response

a illustrates the five parameter measurements used to detect treatment response. We investigated three groups: untreated (UT), anti-PD-1 antibody treated and CD-8 depleted groups. Earlier studies
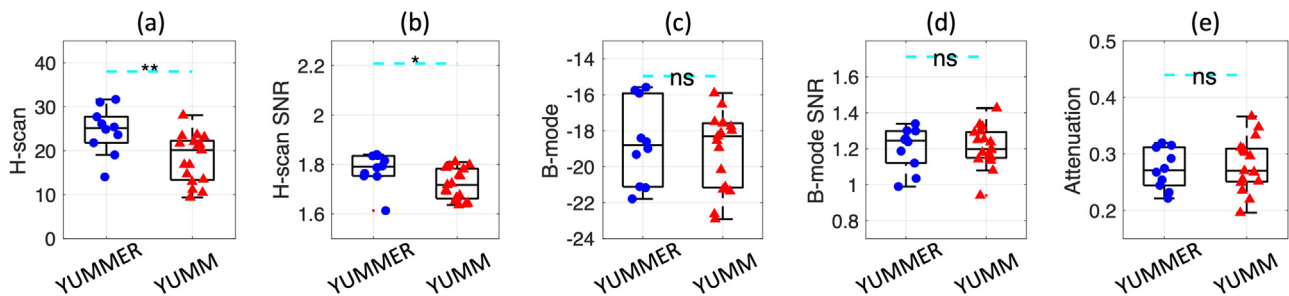

Figure 6. Estimated ultrasound parameters to differentiate YUMMER and YUMM tumors. (a) H-scan % blue. (b) H-scan signal-to-noise ratio (SNR). (c) B-mode intensity (dB). (d) B-scan SNR. (e) Attenuation coefficient (dB/MHz/cm). $*p < 0.05$, $**p < 0.01$, $***p < 0.001$, $****p < 0.0001$. n.s., not significant.
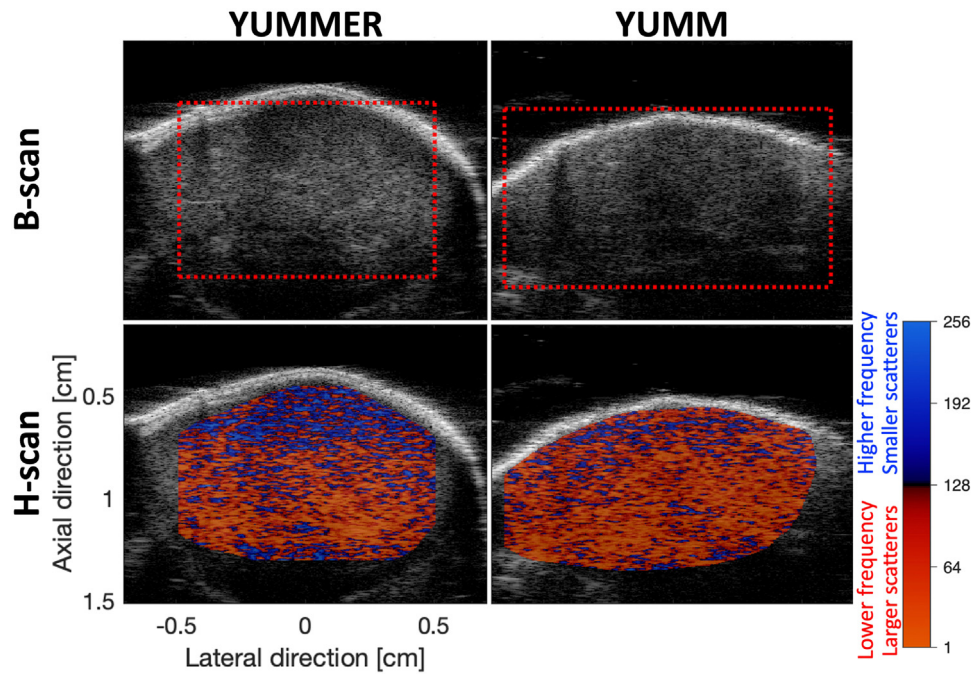
Figure 7. Representative B-scan and H-scan images for YUMMER and YUMM tumors. *Blue* and *red* represent smaller and larger ultrasound scatterers, respectively.
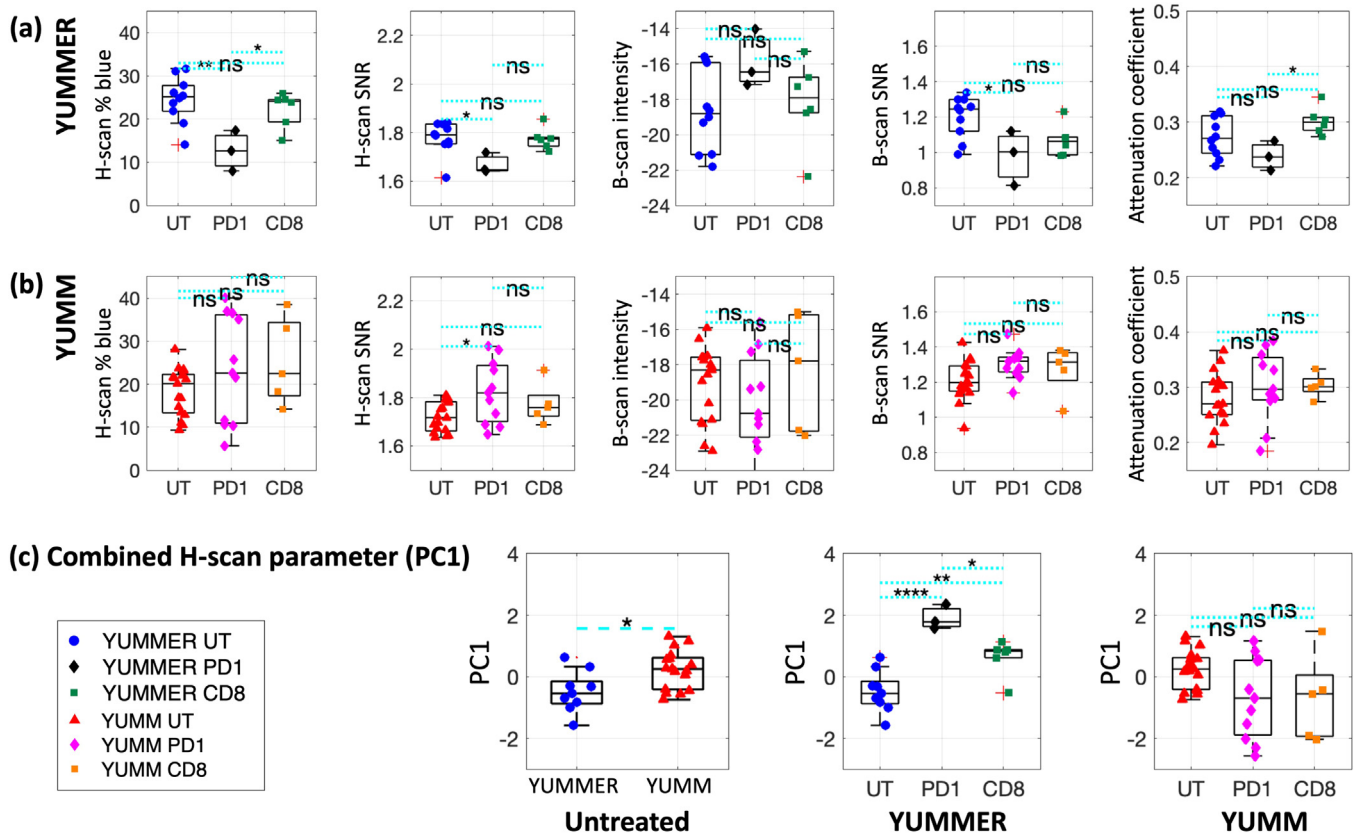

Figure 8. Ultrasound parameters used to investigate treatment response in YUMMER (a) and YUMM (b) tumors. The parameters were H-scan % blue, H-scan SNR, B-scan intensity (dB), B-scan SNR and attenuation coefficient (dB/MHz/cm). The H-scan parameters were combined using principal component analysis (c). The combined parameter (PC1) differentiated YUMMER and YUMM tumors, detected treatment response in YUMMER tumors and showed no response for YUMM tumors. *$p < 0.05$, **$p < 0.01$, ***$p < 0.001$, ****$p < 0.0001$. CD8, CD8 depletion; n.s., not significant; PD1, anti-PD-1 treatment; UT, untreated group.
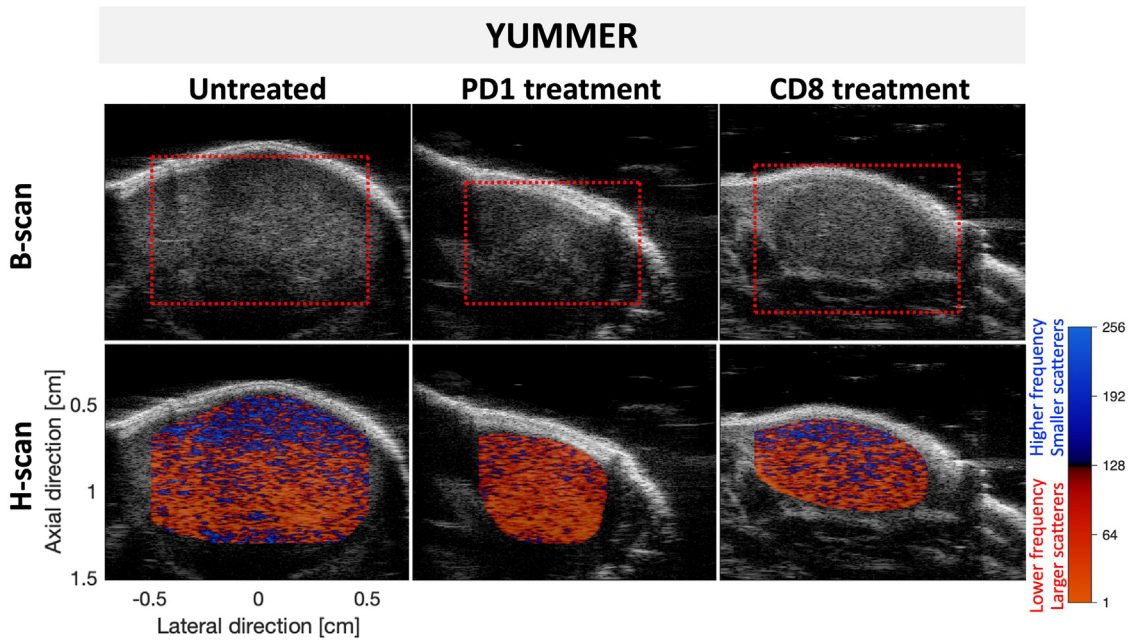
Figure 9. Representative B-scan and H-scan images of YUMMER untreated, PD-1-treated and CD8-treated cases.

determined that anti-PD-1 treatment increased the percentage of CD45+ immune infiltration from approximately 20%−30% to 30%−50%, whereas CD-8 depletion decreased immune infiltration in YUMMER tumors [25−28]. In contrast, immune infiltration into YUMM tumors was not altered by either treatment.

As illustrated in the leftmost plot in Figure 8a, H-scan % blue can detect anti-PD-1 treatment response with a statistically significant difference ($p < 0.01$). Anti-PD-1 treatment caused a red shift (lower % blue), indicating that there was an increase in larger US scatterers caused by the increase in smaller immune cells. Although this may appear inconsistent with histology, clusters of smaller immune cells can convalesce and be read as larger US scatterers in a US echo signal. According to Figure 8a and 8b measurements, these individual parameters tend not to be able to show differences between the three groups. Thus, multiparametric analysis was performed, and the feature selection process found that combining only the two H-scan parameters most accurately described the treatment response. Figure 8c provides the combined H-scan parameter of PC1 derived from

the two H-scan parameters. PC1 indicates a significant difference between YUMMER and YUMM tumors ($p < 0.05$). Moreover, PC1 can detect both anti-PD-1 and CD-8 depletion treatment responses in YUMMER tumors, as demonstrated in the earlier study [25]. According to the study, YUMM was a non-responder to PD-1 and CD8 treatment, which was also found using PC1.

In Figure 9 are B-scan and H-scan images for the responder YUMMER tumors. H-scan can reveal slightly different colors for the cases, illustrating the immunologically distinct TMEs in YUMMER tumors secondary to immune modification treatments.

SVM classification

The H-scan analysis is capable of differentiating YUMMER and YUMM tumors, and it can also detect treatment response for the responder YUMMER tumors. Figure 10 illustrates clustering and classification results in multiparametric space. SVM accurately classified
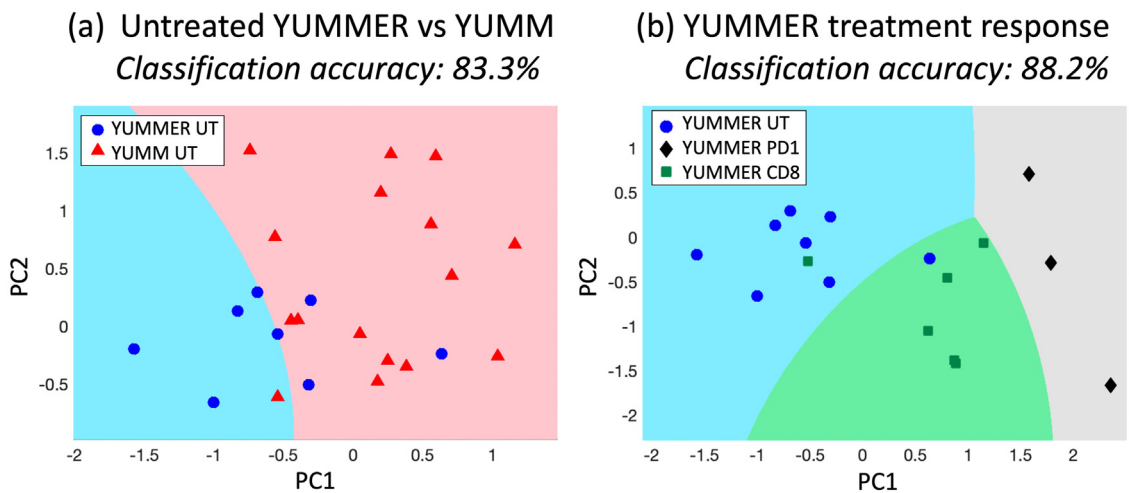

Figure 10. Support vector machine (SVM) classification. (a) Classification between different YUMMER and YUMM forms distinct TMEs with different intra-tumoral immune cell infiltration. (b) Classification between untreated and immunotherapy treated. CD8, CD8 depletion; PD1, anti-PD-1 treatment; TMEs, tumor microenvironments; UT, untreated group.

YUMMER and YUMM tumors (Fig. 10a) and also distinguished treatment groups (Fig. 10b). YUMMER and YUMM tumors can be classified by SVM with 83.3% accuracy. Untreated, anti-PD-1-treated and CD8-depleted YUMMER tumor groups had 88.2% classification accuracy. However, YUMM tumors do not respond to the treatments; measurement in 2-D space revealed overlaps between groups. SVM was not applied to YUMM tumor measurements because the classifier cannot define meaningful hyperplanes without clustered classes.

Discussion

Previous QUS and H-scan studies aimed to discriminate distinct diseases or differentiate the diseased from normal condition [2,5,6,13,14,16,17,19−21,29,30]. However, this study determined that the H-scan is also sufficiently accurate to detect subtle changes within the same type of diseased tissues; the H-scan detected TME heterogeneity between different melanoma tumors. When comparing different types of diseases, morphological pattern differences were likely found in histology images. For instance, fibrosis developed fibrotic septae [19], whereas steatosis generated circle-shaped fat accumulation [14]. In contrast, melanoma metastasis, recapitulated by YUMM and YUMMER murine tumors, may be grossly morphologically identical except for slightly different cellular distributions or sizes measured on a micron scale (Fig. 5). These differences are thus more challenging to detect compared with distinct morphologies of different diseases. In fact, these TME changes were unable to be detected by the widely used B-scan intensity parameters and attenuation coefficient measurements (Figs. 6 and 8). However, H-scan was capable of detecting these cellular differences. Therefore, this study determined the potential of H-scan to be used as a more precise diagnostic tool in assessing subtle changes in the TME, as we revealed the statistically significant differences, with p values <0.05 and high classification accuracies >80%. However, as seen in Figure 10, clusters of YUMMER and YUMM are likely to be overlapped, and YUMMER cases were located near the boundary of SVM hyperplane because of its small number of samples (<10). To define more accurate hyperplanes, future study requires inclusion of a larger data set.

When measuring US features, we have averaged measurements within the entire melanoma lesion, but future studies might include evaluation with localized resolution. Immune cell infiltration can preferentially localize to a specific area or subsequently migrate, causing different immune cell distributions within a lesion. Furthermore, genetic differences between melanoma metastases within an individual host can result in distinct TMEs. These intra-tumoral and inter-tumoral heterogeneities (i) cause difficulties in accurate diagnosis following a single biopsy, (ii) obscure precise immunotherapy selection and (iii) result in differential treatment responses [24,25,31]. Therefore, non-invasive and localized measurement and imaging can contribute to melanoma treatment selection and monitoring. The non-invasive H-scan analysis has pixelwise resolution. Thus, it is necessary to evaluate H-scan accuracy by comparing the same sections imaged by H-scan with histology to verify that the H-scan can precisely illustrate the heterogeneously distributed immune cells within a lesion and between two different lesions.

The number of immune cells for YUMMER tumors were reported in the following order: CD8-depleted < control < anti-PD-1 treated lesions. In contrast, H-scan % blue showed the following order: anti-PD-1 treated < CD8 depleted < control YUMMER tumors. H-scan measurement corresponds to US scatterer sizes; smaller US scatterers result in higher H-scan % blue. The size of most cancer cells has been reported as 10-20 μm, and lymphocytes are generally 5−10 μm in diameter [32−37]. Thus, we can expect the smaller immune cells would result in higher % blue. This was seen in in Figure 7; YUMMER tumors exhibited higher immune cell infiltration than YUMM tumors, resulting in more blue pixels in the YUMMER H-scan image. In addition, when comparing the measurements between the CD8-depleted, which eliminated CD8 + lymphocytes, and the control YUMMER tumors, control YUMMER tumors

resulted in higher H-scan % blue, as expected. However, although anti-PD-1-treated YUMMER tumors had greater immune cell infiltration, they had the lowest % blue values, meaning US scatterers were revealed to be larger with a higher % red. Because of clustering of immune cells, US scatterers in anti-PD-1-treated YUMMER scans can appear larger than single immune and tumor cells. Moreover, the US wavelength was 38.5 μm, and the transducer manufacturer (FUJIFILM VisualSonics, Inc.) has reported its axial resolution is 40 μm. The immune cell size (approximately 5−10 μm) in Figure 5 was found to be smaller than the resolution. Thus, US cannot differentiate single immune cells but only detect changes caused by immune infiltration present in tumor lesions. We can infer that the relatively sparse distribution of the small immune cells can produce more frequent intensity changes for the reflected US echo, acting as smaller US scatterers, whereas the relatively dense distribution of the immune cells with clusters may act as larger US scatterers. Future work could investigate the US scatterer size changes detected by H-scan with varying small cell density. H-scan trajectories along with gradual increase in immune cell infiltration can be studied to monitor melanoma progression.

In this study, five US parameters were extracted from H-scan imaging, conventional B-scan imaging and the attenuation estimation. The H-scan measures detected TME heterogeneity more sensitively than the other parameters. Consistently, previous studies comparing H-scan measures with other parameters, such as attenuation, echo intensity and shear wave elastography parameters, have reported that the H-scan analysis resulted in the most accurate tissue classification [19,20,38]. However, other parameters were still able to differentiate significant differences between diseases (*e.g.*, normal vs. stage 4 steatosis); for example, B-scan, shear wave elastography and H-scan can be used to diagnose severe steatosis [38]. In this study, the only parameters sensitive enough to detect TME heterogeneity were the H-scan parameters (the heterogeneity was not detectable by attenuation or backscattering intensity) because the H-scan uses frequency information, which reflects subtle changes of scatterers. Further, other QUS parameters can be explored to assess melanoma; on the basis of this study, spectral-based approaches, such as spectral slope and mid-band fit, would contribute more than intensity-based approaches, such as the Nakagami parameter. However, the classification performance of parameters can vary depending on the tissue characteristics we aim to detect. When classifying breast cancer, lesion boundary shape is one of the significant factors, which cannot be measured by the H-scan detecting scattering signatures. A breast cancer study reported that boundary shape parameters played the most crucial role in identifying small-sized breast lesions [21]. Therefore, we recommend selecting the H-scan analysis as the most precise metric when detecting US scattering changes. Future study can also include all parameters from H-scan, QUS and shear wave elastography, and compare the performance.

Conclusion

The H-scan analysis was capable of discriminating TME heterogeneity using the murine melanoma models of YUMMER and YUMM tumors. Moreover, the H-scan was sufficiently precise in monitoring changes in immune infiltration following immunomodulatory therapies. These TMEs were not distinguished by other widely used US features. Overall, the H-scan approach is promising in the identification of subtle pathologic changes and has the potential to detect inter-tumoral heterogeneity in melanoma metastases within an individual host, which could ultimately help to individualize immunotherapy selection in metastatic melanoma.

Conflict of interest

The authors declare no competing interests.

Acknowledgments

Data availability statement

Archived data are available on reasonable request.

References

[1] Lee SS, Park SH, Kim HJ, Kim SY, Kim MY, Kim DY, et al. Non-invasive assessment of hepatic steatosis: prospective comparison of the accuracy of imaging examinations. J Hepatol 2010;52:579–85.

[2] Oelze ML, Mamou J. Review of quantitative ultrasound: envelope statistics and backscatter coefficient imaging and contributions to diagnostic ultrasound. IEEE Trans Ultrason Ferroelectr Freq Control 2016;63:336–51.

[3] Kim HC, Al-Mahrouki A, Gorjizadeh A, Sadeghi-Naini A, Karshafian R, Czarnota GJ. Quantitative ultrasound characterization of tumor cell death: ultrasound-stimulated microbubbles for radiation enhancement. PLoS One 2014;9:e102343.

[4] Sharma D, Osapoetra LO, Czarnota GJ. Implementation of non-invasive quantitative ultrasound in clinical cancer imaging. Cancers 2022;14:6217.

[5] Pirmoazen AM, Khurana A, Loening AM, Liang T, Shamdasani V, Xie H, et al. Diagnostic performance of 9 quantitative ultrasound parameters for detection and classification of hepatic steatosis in nonalcoholic fatty liver disease. Invest Radiol 2022:5723–32.

[6] Pirmoazen AM, Khurana A, El Kaffas A, Kamaya A. Quantitative ultrasound approaches for diagnosis and monitoring hepatic steatosis in nonalcoholic fatty liver disease. Theranostics 2020;10:4277–89.

[7] Ozturk A, Grajo JR, Gee MS, Benjamin A, Zubajlo RE, Thomenius KE, et al. Quantitative hepatic fat quantification in non-alcoholic fatty liver disease using ultrasound-based techniques: a review of literature and their diagnostic performance. Ultrasound Med Biol 2018;44:2461–75.

[8] Pineda N, Sharma P, Xu Q, Hu X, Vos M, Martin DR. Measurement of hepatic lipid: high-speed T2-corrected multiecho acquisition at ^{1}H MR spectroscopy—a rapid and accurate technique. Radiology 2009;252:568–76.

[9] Yokoo T, Shiehmorteza M, Hamilton G, Wolfson T, Schroeder ME, Middleton MS, et al. Estimation of hepatic proton-density fat fraction by using MR imaging at 3.0 T. Radiology 2011;258:749–59.

[10] Reeder SB, Cruite I, Hamilton G, et al. Quantitative assessment of liver fat with magnetic resonance imaging and spectroscopy. J Magn Reson Imaging 2011;34: 729–49.

[11] Parker KJ. Scattering and reflection identification in H-scan images. Phys Med Biol 2016;61:L20–8.

[12] Parker KJ, Baek J. Fine-tuning the H-scan for discriminating changes in tissue scatterers. Biomed Phys Eng Express 2020;6:045012.

[13] Baek J, Ahmed R, Ye J, Gerber SA, Parker KJ, Doyley MM. H-scan, shear wave and bioluminescent assessment of the progression of pancreatic cancer metastases in the liver. Ultrasound Med Biol 2020;46:3369–78.

[14] Baek J, Basavarajappa L, Hoyt K, Parker KJ. Disease-specific imaging utilizing support vector machine classification of H-scan parameters: assessment of steatosis in a rat model. IEEE Trans Ultrason Ferroelectr Freq Control 2021;69:720–31.

[15] Baek J, Basavarajappa L, Margolis R, Arthur L, Li J, Hoyt K, et al. Multiparametric ultrasound imaging for early-stage steatosis: comparison with magnetic resonance imaging-based proton density fat fraction. Med Phys doi:10.1002/mp.16648, accessed July 28, 2023.

[16] Baek J, Hysi E, He X, Yuen DA, Kolios MC, Parker KJ. Detecting kidney fibrosis using H-scan. Proc IEEE Int Ultrason Symp (IUS) 2022:1–3.

[17] Baek J, Parker KJ. H-scan trajectories indicate the progression of specific diseases. Med Phys 2021;48:5047–58.

[18] Baek J, Swanson TA, Tuthill T, Parker KJ. Support vector machine (SVM) based liver classification: fibrosis, steatosis, and inflammation. Proc IEEE Int Ultrason Symp (IUS) 2020:1–4.

[19] Baek J, Poul SS, Swanson TA, Tuthill T, Parker KJ. Scattering signatures of normal versus abnormal livers with support vector machine classification. Ultrasound Med Biol 2020;46:3379–92.

[20] Baek J, Poul SS, Basavarajappa L, Reddy S, Tai H, Hoyt K, et al. Clusters of ultrasound scattering parameters for the classification of steatotic and normal livers. Ultrasound Med Biol 2021;47:3014–27.

[21] Baek J, O'Connell AM, Parker KJ. Improving breast cancer diagnosis by incorporating raw ultrasound parameters into machine learning. Mach Learning Sci Technol 2022;3:045013.

[22] Baek J, O'Connell AM, Parker KJ. Breast lesion detection and visualization utilizing artificial intelligence and the H-scan. Proc IEEE Int Ultrason Symp (IUS) 2022:1–4.

[23] Sandru A, Voinea S, Panaitescu E, Blidaru A. Survival rates of patients with metastatic malignant melanoma. J Med Life 2014;7:572–6.

[24] Grzywa TM, Paskal W, Włodarski PK. Intratumor and intertumor heterogeneity in melanoma. Transl Oncol 2017;10:956–75.

[25] Qin SS, Han BJ, Williams A, Jackson KM, Jewell R, Chacon AC, et al. Intertumoral genetic heterogeneity generates distinct tumor microenvironments in a novel murine synchronous melanoma model. Cancers (Basel) 2021;13:2293.

[26] Wang J, Perry CJ, Meeth K, Thakral D, Damsky W, Micevic G, et al. UV-induced somatic mutations elicit a functional T cell response in the YUMMER 1.7 mouse melanoma model. Pigment Cell Melanoma Res 2017;30:428–35.

[27] Meeth K, Wang JX, Micevic G, Damsky W, Bosenberg MW. The YUMM lines: a series of congenic mouse melanoma cell lines with defined genetic alterations. Pigment Cell Melanoma Res 2016;29:590–7.

[28] Qin SS. Effects of intertumoral heterogeneity on immunosuppression and immunotherapy resistance in synchronous melanoma. University of Rochester; 2022.

[29] Baek J, Parker KJ. Disease-specific imaging with H-scan trajectories and support vector machine to visualize the progression of liver diseases. Proc 2021 IEEE Int Ultrason Symp (IUS) 2021:1–4.

[30] Tai H, Song J, Li J, Reddy S, Khairalseed M, Hoyt K. Three-dimensional H-scan ultrasound imaging of early breast cancer response to neoadjuvant therapy in a murine model. Invest Radiol 2022;57:222–32.

[31] Reuben A, Spencer CN, Prieto PA, Gopalakrishnan V, Reddy SM, Miller JP, et al. Genomic and immune heterogeneity are associated with differential responses to therapy in melanoma. NPJ Genom Med 2017;2:10.

[32] Teague TK, Munn L, Zygourakis K, McIntyre BW. Analysis of lymphocyte activation and proliferation by video microscopy and digital imaging. Cytometry 1993;14:772–82.

[33] Pollizzi KN, Waickman AT, Patel CH, Sun IH, Powell JD. Cellular size as a means of tracking mTOR activity and cell fate of CD_4+ T cells upon antigen recognition. PLoS One 2015;10:e0121710.

[34] Rathmell JC, Farkash EA, Gao W, Thompson CB. IL-7 enhances the survival and maintains the size of naïve T cells. J Immunol 2001;167:6869–76.

[35] Tasnim H, Fricke GM, Byrum JR, Sotiris JO, Cannon JL, Moses ME. Quantitative measurement of naïve T cell association with dendritic cells, FRCs, and blood vessels in lymph nodes. Front Immunol 2018;9:1571.

[36] Shashni B, Ariyasu S, Takeda R, Suzuki T, Shiina S, Akimoto K, et al. Size-based differentiation of cancer and normal cells by a particle size analyzer assisted by a cell-recognition PC software. Biol Pharm Bull 2018;41:487–503.

[37] Jiang X, Dudzinski S, Beckermann KE, Young K, McKinley E, McIntyre OJ, et al. MRI of tumor T cell infiltration in response to checkpoint inhibitor therapy. J Immunother Cancer 2020;8:e000328.

[38] Basavarajappa L, Baek J, Reddy S, Song J, Tai H, Rijal G, et al. Multiparametric ultrasound imaging for the assessment of normal versus steatotic livers. Sci Rep 2021;11:1–11.